액적 열전달 향상에 미치는 Dissolved 가스의 영향에 관한 연구

이정호† · Jungho Kim* · Kenneth T. Kiger*

Effect of Dissolved Gases on Liquid Droplet Heat Transfer Enhancement

Jungho Lee, Jungho Kim and Kenneth T. Kiger

Key Words : Liquid Droplet Cooling Heat Transfer, Dissolved Gas, Microscale Heater Array

Abstract

Droplet evaporation can be used to transfer large amounts of energy since heat is transferred across a thin liquid film. Spreading the drop over a larger area can enhance this heat transfer. One method of accomplishing this is to dissolve gas into the liquid. When the drop strikes the surface, a gas bubble nucleates and can grow and merge within the liquid, resulting in an increase in the droplet diameter. In this study, time and space resolved heat transfer characteristics for a single droplet striking a heated surface were experimentally investigated. The local wall heat flux and temperature measurements were provided by a novel experimental technique in which 96 individually controlled heaters were used to map the heat transfer coefficient contour on the surface. A high-speed digital video camera was used to simultaneously record images of the drop from below. The measurements to date indicate that significantly smaller droplet evaporation times can be achieved. The splat diameter was observed to increase with time just after the initial transient dies out due to the growth of the bubble, in contrast to a monotonically decreasing splat diameter for the case of no bubbles. Bursting of the bubble corresponded to a sudden decrease in droplet heat transfer.

1. Introduction

Spray and droplet cooling can be used to extract large amounts of energy at relatively low temperatures through the latent heat of evaporation. Heat transfer rates up to 100 W/cm^2 for FC-72 and 1000 W/cm^2 for water have been demonstrated. One method of enhancing the heat transfer beyond these levels is to add dissolved gas to the liquid so that the splat increases in size as bubbles within the droplet grow, resulting in an increase in the solid/liquid and liquid vapor contact area. The bubble may also cause an increase in heat transfer within the drop, if the liquid film around the bubbles thins locally. Qiao and Chandra (1997) have demonstrated that addition of a surfactant to droplets or sprays can increase the boiling heat transfer by up to 300 %. For temperatures below boiling, the principal effect of the surfactant was to reduce the liquid-solid contact angle, increasing the surface area wetted by liquid. Above the boiling temperature, nucleation occurred at many more sites within the drop and foaming was observed. Cui et al. (2000) studied the effect of dissolved gases or solids on droplet heat transfer. Carbon dioxide gas or a salt was dissolved in water and videos of the evaporation process were obtained as the droplets struck a heated surface. For temperatures below and above the boiling point, the dissolved gas (0.74 mm^3/mm^3) was observed to increase the heat transfer slightly due to an increase in the splat circumference. When 1% by weight of $NaHCO_3$ was added to the liquid, it decayed when heated into Na_2CO_3 and CO_2. Foaming within the droplet was observed to occur along with a large increase in heat transfer. Precipitation of Na_2CO_3 salt within the drop served as nucleation sites for boiling, and the CO_2 produced caused the droplet to swell, increasing the contact area.

Milke et al. (1997) studied the effects of dissolved gas on spray evaporation using water. A Macro substrate was heated using three radiant panels. They found that cooling with gassy liquid resulted in a lower steady-state average temperatures, but attributed this to the decrease of radiant energy input to the surface when gassy liquid was used.

The objective of the current work is to study the fundamental mechanisms by which dissolved gases affect the heat transfer to the drop. Time and space resolved heat

† 삼성코닝정밀유리 유리기술연구소
E-mail : glassman.lee@samsung.com
TEL : (054)470-4022 FAX : (054)470-4387
* Department of Mechanical Engineering
University of Maryland
College Park, MD 20742, USA

transfer characteristics for a single droplet impacting a heated surface were experimentally measured. Small bubbles were observed to form in all of the droplets. In some cases, the small droplets burst and disappeared, while in others they grew and formed a compound drop with a single large bubble (referred to as a primary bubble). The primary bubble burst at different times after droplet impact, which resulted in the droplet evaporation time decreasing by up to 25%. Local wall heat flux and temperature measurements were made using a novel experimental technique in which 96 individually controlled heaters were used to map the heat transfer coefficient contour on the surface. Visual observations of droplet behavior were also made using two high-speed digital video cameras and correlated to the heat transfer data.

2. Experimental Apparatus

An array of 96 individually controlled heaters was used to measure the heat flux distribution on the surface as a function of time and space. Feedback loops similar to those used in constant temperature anemometry were used to vary the voltage across each heater in the array to keep its temperature (resistance) constant, essentially eliminating the possibility of heater burnout. The electronics and heater array allowed for heat fluxes up to 160 W/cm^2. Descriptions of the experimental apparatus are given below.

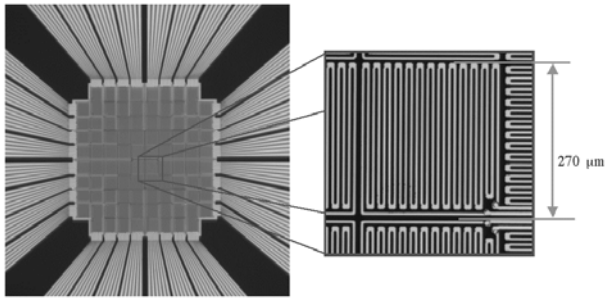

Figure 1. Photograph of microscale heater array.

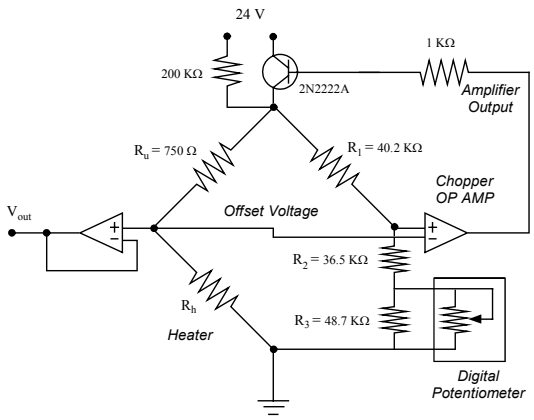

Figure 2. Schematic of feedback circuit.

2.1 Microscale Heater Array

Local surface heat flux and temperature measurements were provided by an array of serpentine platinum resistance heater elements, similar to what was used in previous publications (Rule, et al., 1998, Rule and Kim, 1999, and Rule, et al., 1999). Each heater was 270 μm × 270 μm in size. The platinum heater lines were 5 μm wide, about 400 nm thick, spaced 5 μm apart, and about 600 μm in total length. Each heater had an electrical resistance of about 650 Ω. The 96 individual heaters were arranged in a square array about 2.7 mm on a side.

A photograph of the microscale heater array is shown in Figure 1. The gold leads that supplied power to the heaters were routed between the heaters to the edge of the array. Up to 17 heater arrays were fabricated simultaneously on a single quartz wafer using VLSI circuit fabrication techniques. Platinum was sputtered onto the entire wafer, the heaters were masked off, and the platinum was removed from the unmasked areas using an ion milling process. Gold leads were then deposited on the surface so connections to each individual heater could be made with the feedback electronics (described below). As a final step, a layer of SiO_2 was deposited over the heater array to provide the surface with a uniform surface energy. The completed quartz wafer was diced into chips, each containing a single heater array. The chips were mounted on a pin-grid-array (PGA) package using epoxy adhesive, and the pins of the PGA were connected to the power leads of the heater array chip using a conventional wire-bonding technique. The completed package was then mounted in a PGA socket that was connected to the control and data-acquisition apparatus.

2.2 Feedback Control Circuit

The temperature of each heater in the array was kept at *constant temperature* by feedback circuits similar to those used in constant temperature anemometry (Figure 2). The electronics used in this series of tests were similar to those used in previous tests, and are described in detail in Bae, et al. (1999). The OP-Amp measured the imbalance in the bridge and generated the voltage required to bring the bridge into balance. The heater resistance, and thus the heater temperature, was controlled by varying the resistance of a digital potentiometer from Dallas Semiconductor (DS1267). This chip consisted of two 10 kΩ digital potentiometers, each having 256 wiper positions. The two potentiometers in this chip were connected in series to make a single 20 kΩ potentiometer with 512 wiper positions. Control of the wiper position was performed through a 3-wire serial interface to a personal computer and digital I/O card. For the resistor values indicated, a heater of nominally 750 Ω resistance could be varied over a 105 Ω range. The heaters had a temperature coefficient of resistance of nominally 0.002 °C^{-1}, enabling the temperature to be varied by approximately 70 °C. Since the digital potentiometer had 512 settings, the temperature of the heaters could be changed in 0.15 °C increments. The output of the circuit

(V_{out}) was the voltage required to keep the heater at a set temperature. The heat dissipated by a given heater can be directly obtained from this voltage and the heater resistance. The reader is referred to Bae, et al. (1999) for additional details regarding the circuit.

2.3 Heater Calibration

The heater array was calibrated in an insulated chamber that was held within 0.2 °C of the calibration temperature. Calibration consisted of finding the digital potentiometer wiper position that caused the feedback loop to just begin regulating for a given bath temperature. The uncertainty in threshold wiper position was 1 position, or about 0.15 °C in heater temperature.

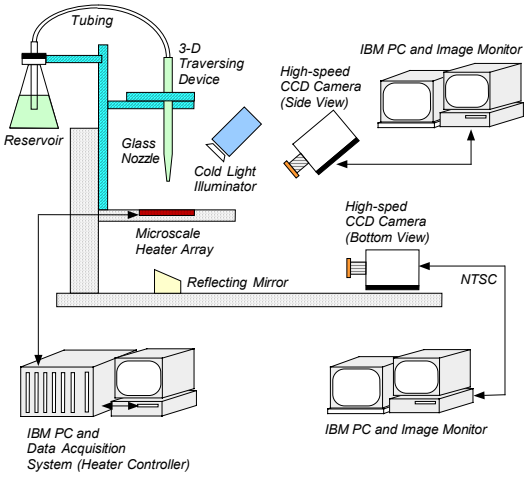

Figure 3. Schematic of test apparatus.

2.4 Test Setup and Data Acquisition System

A schematic of the test apparatus is shown in Figure 3. The drops were produced by allowing fluid to drip from a glass nozzle onto the heater array. The working fluid used in this study was PF-5060, which effectively replaces CFC-113 as a dielectric coolant. This fluid absorbs a large quantity of air, about 48% by volume at room temperature. The boiling temperature for PF-5060 is 56 °C at 1 atm.

The semi-transparent nature of the heater array enabled images to be made of the droplets evaporating on the surface from below using a High-Speed CCD camera (Vision Research Phantom 500 V 3.0) set at 500 fps and 512 × 512 resolution with a 3.5X tele/microscope lens (Infinity Model KC lens with IF4 objective). Pictures were also acquired from a side view using a second high-speed digital video camera at the same settings as the bottom view camera and a second microscope lens (Infinity model K2, with the standard objective). Recording was initiated using the same trigger signal sent to the data acquisition system, allowing heat transfer measurements to be synchronized with the high-speed images. The side-view images were used to calculate the impact velocity by measuring the droplet displacement between successive frames from the high-speed images. The diameter of the splat was measured from both the side-view and the bottom-view of the heater array. Based upon the resolution and depth-of-focus of the images, the uncertainty in the initial drop size and impact velocity is approximately 5%.

The data acquisition system consisted of two A/D boards (ComputerBoards CIO-DAS6402-12) installed in a PC, and was capable of sampling the output of each heater at speeds up to 3.3 kHz with 12 bits of resolution. This system was used to obtain time-resolved data at 3000 samples/sec from each heater for 5.0 seconds. Data acquisition was triggered by the rising edge of a TTL signal from the computer and data was stored to disk.

3. Data Reduction and Uncertainty Analysis

The instantaneous power required to keep each heater at a constant temperature was measured and used to determine the heat flux from each heater element. The energy dissipated within an individual heater, q''_{raw}, can be divided into three different energy sinks:

1) q''_{liq}, the heat transferred to the liquid drop, which is the measurement goal of the current study,
2) q''_{nc}, the heat lost to natural convection on the area not covered by the liquid,
3) q''_{sc}, the heat lost due to substrate conduction out the sides and bottom of the quartz substrate.

In all of the cases studied, q''_{nc} was much smaller than either q''_{sc} or q''_{liq} and could be neglected. Before the droplet impacted the heater array, the power supplied to each heater was lost only by substrate conduction. As a result of the heaters being held at constant temperature, the substrate conduction remained constant even after droplet impact, enabling the heat transferred from the heaters to the liquid to be determined by subtracting q''_{sc} from q''_{raw}.

The uncertainty in the final heat flux values resulted from uncertainties in q''_{raw}, q''_{nc}, and q''_{sc}. Uncertainties in q''_{raw} were relatively small since they were computed directly from the measured voltage across the heaters and since the heater resistances did not change much. The maximum uncertainty in the voltage across the heater was 0.02 V. The uncertainty in heater resistance was about 1 Ω. Since the heater resistance was nominally 750 Ω, the % uncertainty in heater resistance was about 0.14 %.

The uncertainty of the local heat flux measurements was estimated for a typical heater voltage of 2 V using the method suggested by Kline and McClintock (1953). The estimated uncertainty in q''_{raw} was about 2 %. The uncertainties in q''_{nc} and q''_{sc} were estimated to be about 5 % and 2 %, respectively. The uncertainty in q''_{nc} could be large, but it contributed very little to the final uncertainty, since the actual value of q''_{nc} was very small compared to q''_{sc} (q''_{nc} was about 5 % of that of q''_{sc}). The final uncertainty in the heat flux to the liquid drop was therefore small, and is approximately 4%. The uncertainty in droplet diameter (4%) translated into a much larger un-

certainty when computing the energy required to evaporate it because of the dependence on d_o^3.

4. Results and Discussion

The experiments were conducted with the heater array set at 65 °C. The release height of the droplets was kept constant at approximately 2.8 mm and impacted the heater array with a nominal velocity of 0.23 m/s. The droplets pinched off from the glass nozzle with diameter of 0.82 mm, and were initially at a temperature of 25°C. A summary of the droplet initial conditions and evaporation times for four of the droplets that struck the surface is given in Table 1.

Table 1 Summary of droplet initial conditions and evaporation times for four drops.

Case	Droplet diameter, D (mm)	Droplet evaporation time, t_e (s)	Comments
T65_1	0.82	1.01	No primary bubble
T65_2	0.82	1.02	No primary bubble
T65_4_b	0.82	0.884	Primary bubble bursting at 0.484 s
T65_6	0.82	0.75	Primary bubble bursting at about 0.6 s

Table 2 Summary of droplet initial conditions and evaporation times for four drops.

Case	Droplet diameter, D (mm)	Total energy, Q (J)	Equivalent Diameter, D_{eq} (mm)	$\frac{D}{D_{eq}}$
T65_1	0.82	0.0561	0.829	1.00
T65_2	0.82	0.0596	0.826	0.99
T65_4_b	0.82	0.0613	0.8336	0.98
T65_6	0.82	0.0603	0.829	0.99

4.1 Energy Balance

The energy transferred from the wall to the drop can be obtained by integrating the measured wall heat transfer over all the heaters and the entire droplet evaporation time:

$$Q = \sum_{t=0}^{t=t_e} \sum_{i=1}^{i=N} q_i''(t) A_i \Delta t$$

This energy can be converted into an equivalent droplet diameter (d_{eq}) using an energy balance on the drop

$$Q = \rho_d \pi \frac{d_{eq}^3}{6} \left[c_p (T_{sat} - T_0) + h_{fg} \right]$$

The ratio of d_o to d_{eq} is given on Table 2. This ratio is very close to unity, verifying that the measurements are accurate to within the specified uncertainty in the diameter measurements (4%).

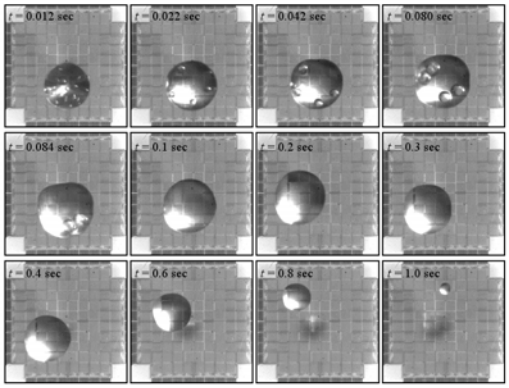

Figure 4. Image sequence showing droplet evaporation for case T56_1, with no large bubble formation.

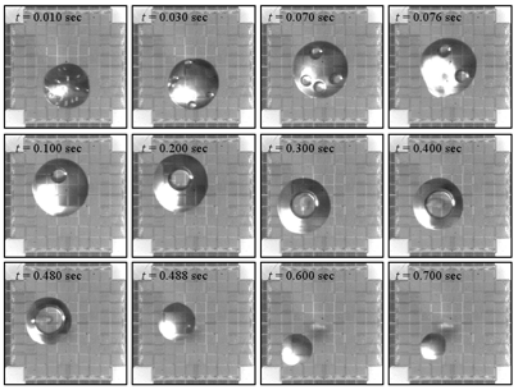

Figure 5. Image sequence showing droplet evaporation for case T56_4b, with large bubble formation.

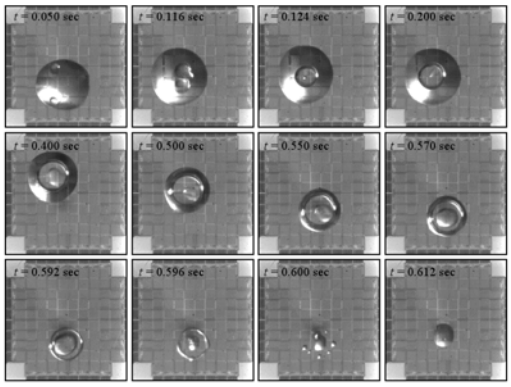

Figure 6. Image sequence showing droplet evaporation for case T56_6, with large bubble formation.

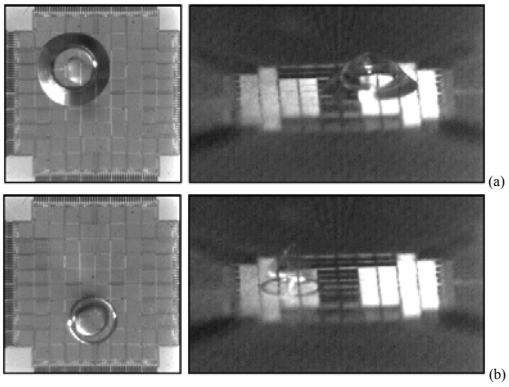

Figure 7. Bottom and side view of compound drop and bubble for case T56_6 at (a) t = 0.400 and (b) t = 0.592 seconds. In (b), most of the liquid phase has condensed on the upper surface of the bubble, leaving it suspended by only a thin membrane above the heater surface.

4.2 Droplet Flow Visualization

Images of the droplet behavior recorded using the bottom and side-view high-speed cameras are shown in Figures 4-6.These images revealed that the droplets had a nominally similar initial history during the first 0.05 seconds, which was characterized by:

1) two to three oscillations in drop shape and surface area caused by the drop's impact on the substrate before being damped out by viscous dissipation
2) the formation of numerous small bubbles, which successively grew, burst, and/or coalesced.

After this early stage of the drop vaporization, the process then evolved according to one of two scenarios that result in a significant difference in the total lifetime of the droplet. In the first mode, all of the smaller bubbles that were formed shortly after impact burst, leaving the liquid drop free of voids. Case T65_1 is typical of these droplets, and several selected images from this case is shown in Figure 4. In the initial spreading of the drop, as many as 20 to 30 small bubbles about 50 m in diameter form and rapidly burst or coalesce in the first 15 ms. By 0.022 s, only five bubbles remain, which have now grown to approximately 150 to 200 m in diameter. These bubbles then remain in the droplet and continue to grow, until they also burst during attempted coalescence at t = 0.08 s past the initial drop impact. It appears that the disturbance generated by the bursting of one pair of bubbles destabilized the last remaining pair, which finally burst about 0.084 s after impact. The oscillations caused by these bursting events are damped by t = 0.1 s, and the droplet assumed an approximately spherical cap shape for the remainder of its lifetime.

In the second mode of droplet vaporization, the smaller initial bubbles coalesce into a single primary bubble that survives and grows through a significant portion of the drop lifetime. Cases T65_4b and case T65_6 are examples of two drops that exhibited this behavior, and select images from their evolution are shown in Figures 5 and 6. For case T65_4b (Figure 5), the primary bubble has survived the cascade of rupture events that occur between t = 0.075 s to 0.080 s. At t = 0.2 s, this bubble has migrated toward the center of the droplet, and has already grown in size to approximately 0.5 mm in diameter. By t = 0.3 s, distortions are visible on the bubble that are likely film draining instabilities that result from vapor condensing on the upper inside surface of the bubble. This distortion is clearly visible when the bubble is larger than 0.5 mm, and typically undulates around the periphery of the bubble. The side-view images reveal that no distortion is visible on the outside of the bubble, indicating that the interface is being distorted only within the bubble. Additional discussion regarding this point is given below. At t = 0.484 s, the primary bubble bursts, and liquid rapidly coalesces into a small spherical cap, which then evaporates according to the first mode of droplet evaporation.

The early history of drop T65_6 (Figure 6) is qualitatively similar to that of case T65_4b, with the exception that the primary bubble results from the coalescence of two smaller bubbles at t = 0.116 s. An insufficient number of droplets have been examined in order to determine the factors influencing the survival or demise of the bubbles within the drop. However, in these two cases, the primary bubble results from either an isolated bubble that survives the disturbances generated by its neighbors during collapse, or from the coalescence of two bubbles near the center region of the drop. As in the T65_4b case, the primary bubble continues to grow, and appears to have condensation and film drainage occurring inside the bubble after reaching a size of approximately 0.5 mm. Unlike the T65_4b case, the bubble survives over 0.1 s longer, resulting in a remarkable decrease in the overall lifetime of the droplet (see Table 1). Another interesting feature about this case is that around t = 0.55 s, the wetted area surrounding the droplet appears to rapidly thin, leaving a smaller contact surface area in which to support the bubble. At the same time, the liquid film draining from the upper surface of the drop appears to temporarily stabilize, and accumulate in the form of a pendant drop within the bubble. This can be observed in the side-view images as shown in Figure 7 at t = 0.592 s. By t = 0.594 s, the bubble has burst. Part of the pendant droplet falls down onto the heated surface and part is ejected upward, while the bubble thin film has collapsed around the base and broken into a series of smaller satellite droplets around the periphery. The part of the pendent that is ejected upward impacts onto the surface at t = 0.604 s and coalesces with the part ejected downward. Following the rapid vaporization of the satellite droplets, the remaining liquid appears to evaporate in a manner similar to the first mode of evaporation.

As a final note, no liquid was ejected outside the heated area during the bursting event of the bubbles. Although eject was observed during the collapse of the larger bubbles, the drops landed in the confines of the heated space for all of the results presented here. This

was also confirmed from the energy balances determined from the measured heat input into the array.

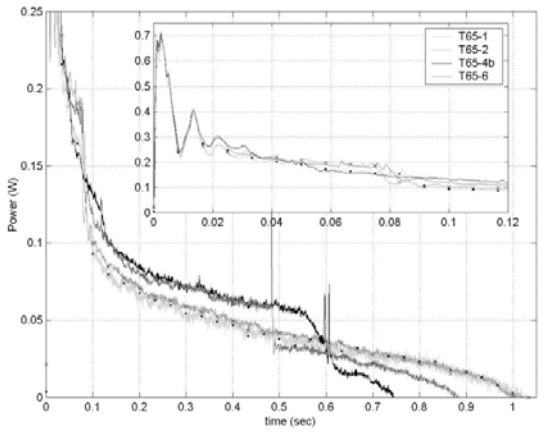

Figure 8. Total power dissipated to droplet as a function of time for four different cases.

4.3 Time Resolved, Space Averaged Heat Transfer

The time-resolved heat transfer variation from the array for all of the cases are shown in Figure 8. The ordinate was obtained using the following equation:

$$q(t) = \sum_{i=1}^{i=N} q_i''(t) A_i$$

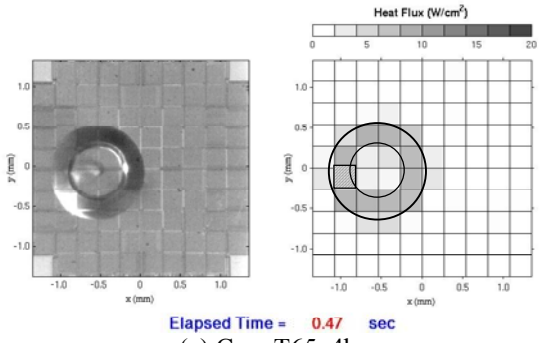

(a) Case T65_4b

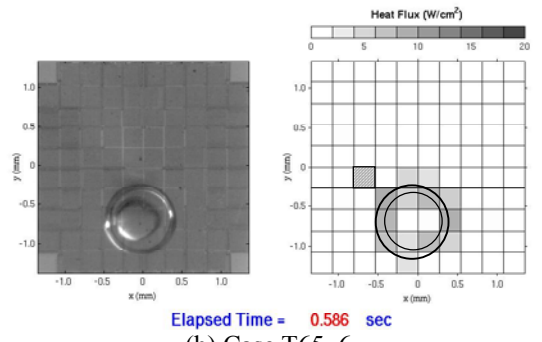

(b) Case T65_6

Figure 9. Examples of time and space resolved wall heat transfer showing low heat transfer under the primary bubble. The cross-hatched heater is non-functional.

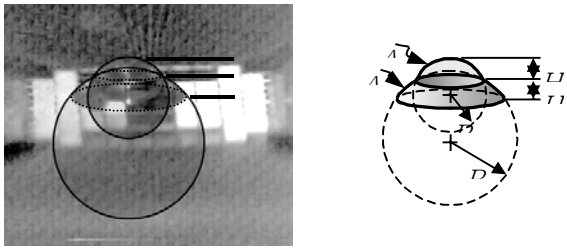

Figure 10. Sketch showing the measurement of the liquid-vapor surface area for compound droplet/bubble.

where $q_i''(t)$ is the wall heat flux at time t for heater i corrected for substrate conduction.

The heat transfer rates shortly after impact (Figure 8 inset) are remarkably repeatable from drop to drop. The oscillations in heat transfer are associated with the spread and recoil of the droplet during the initial transient. The large heat transfer values are most likely associated with transient conduction and micro-convection within the droplet as it heats up from room temperature.

The heat transfer curves decay at different rates after the initial transient dies out, however, with the droplet evaporation time depending mainly on the time at which the primary bubble bursts. The bubbles for cases T65_1 and T65_2 all burst by t = 0.1 s, after which the heat transfer varies similarly with time for the remainder of the evaporation process. The heat transfer variation for the two cases in which a primary bubble forms (T65_4b and T65_6) are similar until bursting occurs for T65_4b at t = 0.49 s. Case T65_4b shows a case in which the bursting of the bubble is associated with a brief spike in the wall heat transfer, followed by an abrupt decrease of almost 50%. Comparison of the curves with and without the primary bubble clearly indicates that the heat transfer when a primary bubble is present on the surface is higher than without the primary bubble. It is evident from energy balance considerations that this must result in a shorter droplet evaporation time. Case T65_6 shows a gradual drop in wall heat transfer between 0.55 s until bubble burst just after 0.592 s. The reason for this behavior is discussed below. A spike in heat transfer is observed when the bubble bursts. A second spike in heat transfer centered around 0.606 s occurs when the liquid ejected upward during bubble burst impacts the surface.

There are two possible mechanisms by which a shorter evaporation time can result when a primary bubble is present. First, the bubble can cause the drop to spread out, increasing the Liquid-Solid Contact Area (LSCA) and therefore the heat transfer. Second, the bubble can increase the Liquid-Vapor Contact Area (LVCA) on top of the drop, enabling vapor to diffuse away more rapidly. Previous work by Qiao and Chandra (1997), di Marzo et al. (1993), and Milke et al. (1997) has suggested that both of these mechanisms are important, but that the limiting factor in droplet evaporation was likely the vapor removal rate.

Measurements of LSCA and LVCA were obtained from bottom and side view images, respectively, of the

droplet evaporation process. The LSCA was obtained from the splat and bubble diameters. The splat diameter, D_s, was measured from the edge-to-edge distance in two orthogonal directions from the bottom view and averaged. When a primary bubble formed on the surface (Figure 6 and 7), it was assumed that a dry patch existed under the bubble. The presence of a dry patch is supported by space resolved heat transfer measurements as shown on Figure 9. A region of very low heat transfer is observed on the heaters that are completely enclosed within the bubble projected area. Some of the heaters are partially covered by the primary bubble, and these show a higher heat transfer. The diameter of this dry area was measured from the apparent diameter of the bubble ($D_{b,i}$), which was used to compute the LSCA as follows:

$$\text{LSCA} = \frac{\pi}{4}\left(D_s^2 - D_{b,i}^2\right)$$

The Liquid-Vapor Contact Area (LVCA) was estimated from the side view images by fitting a circle to the upper surface of the droplet, measuring the height of the droplet, and assuming that the surface had the shape of a spherical segment. For simple drops (no bubble) this area is given by (Råde & Westergren, 1995):

$$\text{LVCA} = 2\pi R_d H_d$$

where R_d is the radius of the spherical segment (which is different from the radius of the wetted liquid-solid contact area, D_s / 2), and H_d is the height of the segment. For compound drops (cases with a single large bubble), the LVCA is estimated by assuming that both the bubble and the drop are spherical segments, and are fit with two circles; one to the bubble, and one to the liquid base drop (see Figure 10). Measuring the height of each segment (H_d and H_b for the drop and bubble, respectively), the LVCA is then calculated by:

$$\text{LVCA} = A_d + A_b = 2\pi\left(R_d H_d + R_b H_b\right)$$

For cases with numerous smaller bubbles, a single sphere was fit to the overall shape. Distortions caused by these bubbles, and the oscillations of the drops during the early impact history prevented the reliable estimate of the LVCA prior to t = 0.1 sec.

A comparison of both the LSCA ratio and the LVCA ratio to the temporal evolution of the total heat transfer rate is shown on Figure 12. For case T65_1, in which no bubble is present, it can be observed that both the LSCA and the LVCA (Figure 12a and 12b) track the heat transfer rate closely over most of the droplet lifetime. The exception to this is for t < 0.2 s, where the area ratio for the LSCA and the LVCA is distinctly below the trend for the heat transfer rate. The close agreement between the two values to the heat transfer for the drop without bubbles is not surprising – the geometry of the drop corresponds closely to a segment of a sphere during the evaporation and the minimum (receding) contact angle has been reached, fixing the proportion between the LVCA and the LSCA. This is not the case for the compound drops, however, as shown for cases T65_4b and T65_6 in Figure 12c-f. In these cases, the presence of the bubble increases slightly the maximum diameter of the splat as a result of the surface tension forces on the bubble. During the middle of the droplet's existence, however, the LSCA actually begins to decrease below the heat transfer curve at approximately t = 0.35 seconds. The LVCA, on the other hand, continues to track the heat transfer faithfully, and even matches the discontinuous jump that occurs just after the bubble bursts in case T65_4b at t = 0.484 seconds. For case T65_6, the LVCA also tracks quite well the gradual reduction that is induced by the growth of the primary bubble, whereas the LSCA is already 50 to 70% below the corresponding area ratio that would be required if the heat transfer were governed predominantly by the contact area with the solid surface.

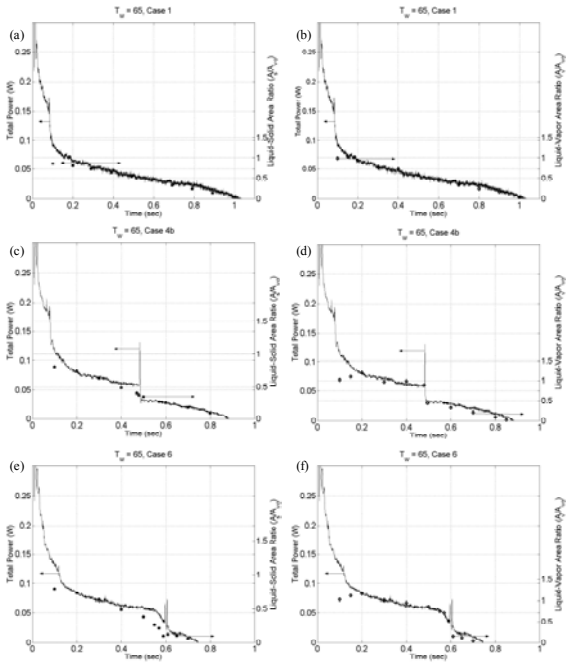

Figure 11. Total heat transfer rate history compared with different contact areas for different cases. (a) case 1, LSCA; (b) case 1, LVCA; (c) case 4b, LSCA; (d) case 4b, LVCA; (e) case 6, LSCA; (e) case 6, LVCA.

4.4 Heat Transfer Coefficients

The heat transfer coefficient is given by

$$h(t) = \frac{q(t)}{A\left(T_w - T_a\right)}$$

In the present work, $q(t)$ is measured while the temperature difference if fixed since the wall temperature is fixed. However, it is not obvious what the area A should be, however. Three areas that could be used are the drop-

let projected area (total area within the outer contact line), the LSCA, and the LVCA. Plots of the variation in $h(t)$ based on these areas are shown on Figure 12. It can be observed that defining h(t) on the LVCA results in relatively small variations after the initial transient, particularly before and after the bubble burst. The droplet projected area and the LSCA do not faithfully track the variations in heat transfer when a primary bubble is present, as was indicated by the comparison in Figure 11. Defining a heat transfer coefficient based on LVCA, while not practical, does indicate that the LVCA is the controlling mechanism for droplet evaporation.

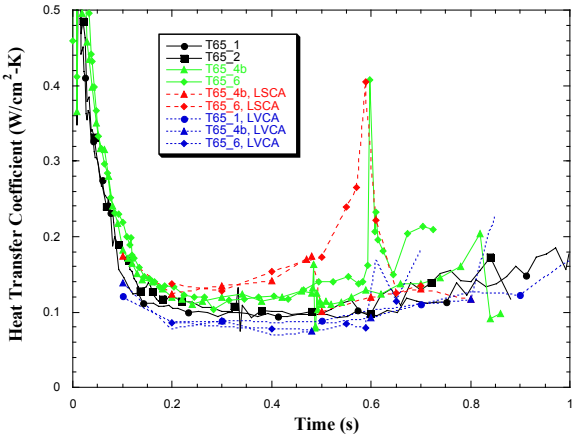

Figure 12. Heat transfer coefficient variation.

5. Conclusion

An experimental technique using an array of microscale heaters and high-speed imaging has been used to examine the time and space resolved heat flux and dynamics of the droplet vaporization process on an isothermal wall. The experiments were performed with a working fluid of PF-5060 in ambient air, with a fixed impact diameter (0.82 mm) and velocity (0.23 m/s). Data was obtained on drops in which the bubbles burst very soon after impact, as well as in which a large primary bubble formed within the drop and burst at various times during the evaporation process. Formation of bubbles within the drop was found to increase the wall heat transfer and decrease the drop lifetime. The wall heat transfer due to an evaporating drop was found to be primarily dependent to the liquid-vapor contact area, indicating that the vapor removal process is the limiting thermal resistance.

Acknowledgments

This work was jointly supported by the Air Force Research Laboratory (AFRL), Wright Patterson Air Force Base, Dayton, OH under the grant F33615-98-1-2791 and the Laboratory for Physical Sciences (LPS), College Park, MD. The authors wish to express their gratitude to Dr. R. Ponnappan (AFRL) and Dr. P. Boudreaux (LPS) for their encouragement and support throughout this study.

References

(1) Bae, S., Kim, M. H., and Kim, J., 1999, "Improved Technique to Measure Time and Space–Resolved Heat Transfer under Single Bubbles during Saturated Pool Boiling of FC-72," *Experimental Heat Transfer*, Vol. 12, pp. 265-278.

(2) di Marzo, M., Tartarini, P., Liao, Y., Evans, D., and Baum, H., 1993, "Evaporative Cooling Due to a Gently Deposited Droplet," *International Journal of Heat and Mass Transfer*, Vol. 36, pp. 4133-4139.

(3) Kline, S. J., and McClintock, F. A., 1953, Describing Uncertainties in Single-Sample Experiments, *Mechanical Engineering*, Vol. 75, pp. 3-8.

(4) Lee J., Kim, J., and Kiger, K. T., 2001, "Time and Space Resolved Heat Transfer Characteristics of Single Droplet Cooling Using Microscale Heater Arrays," *International Journal of Heat and Fluid Flow*, Vol. 22, pp. 188-200.

(5) Milke, J.A., Tinker, S.C., and di Marzo, M., 1997, "Effect of dissolved gases on spray evaporative cooling with water," *Fire Technology*, 2nd Quarter, Vol. 33, No. 2, May/June.

(6) Q. Cui, S. Chandra, S. McCahan, 2000, "Enhanced boiling of water droplets containing dissolved gases or solids", Paper No. NHTC 2000-12249, *National Heat Transfer Conference*, Pittsburgh, Pennsylvania, August 20-22.

(7) Qiao, Y. M. and Chandra, S., 1997, "Experiment on Adding a Surfactant to Water Drops Boiling on a Hot Surface," *Proceedings of Royal Society of London A*, Vol. 453, pp. 673-689.

(8) Råde, L. and Westergren, B., 1995, *Mathematics Handbook for Science and Engineering*, Birkhäuser, Sweden.

(9) Rule, T. D., Kim, J., and Kalkur, T. S., 1998, "Design, Construction, and Qualification of a Microscale Heater Array for Use in Boiling Heat Transfer," NASA/CR-1998-207407.

(10) Rule, T. D., and Kim, J., 1999, "Heat Transfer Behavior on Small Horizontal Heaters During Pool Boiling of FC-72," *Journal of Heat Transfer*, Vol. 121, pp. 386-393.

(11) Rule, T. D., Kim, J., Quine, R. W., Kalkur, T. S., and Chung, J. N., 1999, "Measurements of Spatially and Temporally Resolved Heat Transfer Coefficients in Subcooled Pool Boiling," *Convective Flow and Pool Boiling*, Taylor and Francis.